The Oxysulfide Ba 5 (VO 2 S 2) 2 (S 2) 2 Combining Disulfide Channels and Mixed Anion Tetrahedra and its Third Harmonic Generation Properties

Batoul Almoussawi, Marielle Huvé, Valérie Dupray, Simon Clevers, Victor Duffort, Olivier Mentré, Pascal Roussel, Angel Arevalo Lopez, Houria Kabbour

The Oxysulfide $Ba_5(VO_2S_2)_2(S_2)_2$ Combining Disulfide Channels and Mixed Anion Tetrahedra and its Third Harmonic Generation Properties

Batoul Almoussawi[1], Marielle Huvé[1], Valérie Dupray[2], Simon Clevers[2], Victor Duffort[1], Olivier Mentré[1], Pascal Roussel[1], Angel M. Arevalo-Lopez[1], Houria Kabbour[1]*

[1] *Univ. Lille, CNRS, Centrale Lille, ENSCL, Univ. Artois, UMR 8181 – UCCS – Unité de Catalyse et Chimie du Solide, F-59000 Lille, France*

[2] *Normandie Univ, UNIROUEN, SMS, 76000 Rouen, France*

*houria.kabbour@univ-lille.fr

Abstract

Mixed anion compounds are among the most promising systems to design functional materials with enhanced properties. In particular, heteroleptic environments around transition metals allow tuning of polarity or band gap engineering for instance. We present the original oxysulfide $Ba_5(VO_2S_2)_2(S_2)_2$, the fifth member in the quaternary system Ba-V-S-O. It exhibits the mixed anion building units $V^{5+}O_2S_2$ and isolated disulfide pairs $(S_2)^{2-}$. The structure is solved by combining single crystal and powder X-Rays Diffraction (XRD) and transmission electron microscopy (TEM). First-principles calculations were combined in order to highlight the anions roles. In particular, our DFT study shows that the 3*p* states of the disulfide pairs dictate the band gap. In this study, we point out *anionic* tools for band gap engineering, which can be useful to design phases for numerous applications. Finally, third Harmonic Generation (THG) was measured and compared to the large THG observed for Cu_2O, which reveals potentialities for non-linear optical properties that should be further investigated.

Introduction

Mixed anion compounds are among the most promising systems for the prospection of original phases and for the control/enhancement of functionalities. Despite this matter of fact,

they remain less explored compared to single anion phases and in particular compared to oxides. A recent review[1] highlights the great interest of heteroleptic environments around transition metals (O^{2-}, S^{2-}, N^{3-}, H^-, F^- *etc*….) compared to oxides for numerous properties such as visible light photocatalysis[2], batteries[3], thermoelectricity[4], magnetism[5, 6] *etc. …* In that context, oxysulfides represent a remarkable family that opens several perspectives in various domains. For instance, layered oxychalcogenides are emerging as potential tunable thermoelectrics[7] thanks to the stack of versatile ionic oxide and more covalent chalcogenide layers. The contribution of the chalcogenide anion in the emergence of visible light photocatalytic activity is also promising such as in $LaOInS_2$ [8a] and its polymorph α-$LaOInS_2$ for water splitting [8b]. It is important here to highlight the powerful "anionic" tool for band gap engineering. Indeed, solar water-splitting photocatalysis requires a band gap in the range 3.1 eV – 1.23 eV while the potential of the conduction band (CB) and of the valence band (VB) should encompass the reduction and oxidation potentials of water. The interplay between multiple anions is determinant for these crucial aspects, thus opening the route for the rational design of functional materials. On another hand, while the band gap can be tuned by the concomitant contribution of different anionic species[9], local geometric effects can benefit to nonlinear optical (NLO) materials[10]. For instance, the polar phase $SrZn_2S_2O$ with ZnS_3O building blocks[11], forming unusual Wurtzite-like slabs, is the first phase matchable NLO oxysulfide and exhibits a large Second Harmonic Generation (SHG) response twice the KDP reference material one. Here, the heteroleptic building units have a more pronounced acentric character, then their polar arrangement lead to an enhanced dipolar momentum which directly impact the related properties. While second order nonlinear optical processes are observed in systems without inversion symmetry, the third order ones may be observed in any medium, centrosymmetric or not. In Third Harmonic Generation (THG), three photons interact together to give rise to new photon at the third of the fundamental wavelength ($\lambda/3$) (*i.e.* the frequency is triple)[12]. THG processes offer the possibility to extend the frequency conversion processes. In particular, materials allowing THG can be used to generate directly (and not via a series of second order NLO processes) coherent laser light in the UV region from commercially available laser sources[13]. Such UV sources are highly demanded in a variety of applications such as medical applications, short-range optical communication or chemical sensing. They have also potential interest in quantum optics with possible direct generation of photon triplets from the reverse process of THG[14]. THG has been investigated for instance

on the centrosymmetric rutile oxide TiO_2 ($P4_2/mnm$) with efficient triple photon generation[15]. We find such phenomenon in a new mixed anion phase, the centrosymmetric oxysulfide $Ba_5(VO_2S_2)_2(S_2)_2$, which we present here. Its original structure is made of heteroleptic (VO_2S_2) tetrahedra and of disulfide pairs forming a one-dimensional arrangement. Here we present the structure; the DFT computed electronic structure and the THG properties which are rarely investigated for this type of materials. It represents the fifth original phase reported in the quaternary system Ba-V-S-O. We analyze this phase's electronic structure in relation with the structural units building it. It opens interesting perspectives for the band gap engineering of inorganic compounds from mixed anionic matrices, including disulfide pairs.

Experimental section

Synthesis: Single crystals of $Ba_5(VO_2S_2)_2(S_2)_2$ (i.e. $Ba_5V_2O_4S_8$) were initially found during an exploratory synthesis that included the elements Ba-V-O-S. We attempted to synthesize a single phase material from a mixture of the precursors BaS/BaO/V/S in the molar ratio 1:4:2:7. Those precursors were mixed and thoroughly ground in an agate mortar before being pressed into pellets and heated in an evacuated sealed quartz tube. The heat treatment consisted in heating up to 400°C at a rate of 35°C/h for 10 hours, then to 800°C at a 50°C/h rate for 96 hours, before cooling down to 600°C at a 20°C/h rate, temperature at which the furnace was switched off.

X-ray diffraction on single crystals diffraction was performed on an X8 diffractometer equipped with a bi-dimensional CCD 4K detector and an Ag K_α source.

Electron diffraction study was performed on a FEI Technai G2-20 twin TEM microscope. The powder was crushed and dropped in the form of alcohol suspension on carbon supported copper grids followed by evaporation under ambient condition.

The powder X-ray diffraction pattern was collected on a Bruker D8 diffractometer equipped with a linear detector Lynxeye ($Cu_{K\alpha}$) in Bragg-Brentano geometry at room temperature.

DFT calculations were carried out by employing the projector augmented wave (PAW)[16, 17] method encoded in the Vienna ab initio simulation package (VASP)[18] and the generalized gradient approximation of Perdew, Burke and Ernzerhof[19] (PBE) for the exchange-correlation functionals. The full geometry optimizations were carried out using a plane wave energy cutoff

of 550 eV and 12 *k* points in the irreducible Brillouin zone. It converged with residual Hellman-Feynman forces on the atoms smaller than 0.03 eV/Å and led to a good match with the experimental structure, i.e. within a reasonable error expected for the GGA method. The relaxed structure was used for calculations of the electronic structure. For the later, the plane wave cutoff energies of 550 eV and the threshold of self-consistent-field energy convergence of 10^{-6} eV were used, with 90 *k* points in the irreducible Brillouin Zone.

Scanning electron microscopy (SEM) experiments and EDX analysis were carried out on a Hitachi S400N.

UV-Visible measurements: The reflectance of the sample was measured from 250 to 800 nm on a Perkin Elmer Lambda 650 device.

The thermogravimetric analysis (TGA) where conducted on a TGA-92 thermobalance (Setaram) under synthetic air (N_2/O_2 80%/20%) and pure argon. The evolved gases were monitored by an Omnistar quadrupole mass spectrometer (Pfeiffer) by continuously scanning in the range 0 – 100 amu. In order to control the atmosphere, the whole thermobalance was evacuated and filled with the carrier gas before heating up the samples up to 800 °C at a rate of 5 K/min.

Non-linear optical measurements

Insight X3 single laser with automated dispersion compensation (Spectra-Physics, Santa Clara, USA) and a TCS SP8 MP confocal microscope (Leica Microsystems, Wetzlar, Germany) have been used to perform confocal microscopy as well as two-photon microscopy analyses of the samples. The laser delivers over 2.54 W of average power at 900 nm and is tunable from 680 nm to 1300 nm. The repetition rate is 80 MHz and the temporal width at the output of the cavity is around 120 fs (<100fs between 850 nm and 1050 nm). The laser is controlled with the LASX Leica software. Two Leica hybrid descanned detectors (HyD) were used to record images. For two-photon imaging experiments, fluorescence was collected after the microscope objective via a dichroic beamsplitter, transparent to wavelengths greater than 815 nm. Microscope objectives were long working distance dry Leica objectives (HC PL Fluotar 5X NA 0.15, HC PL Fluotar 10X NA 0.3 or HC PL APO 20X NA 0.4 CS2) or oil- immersion Leica objective (HC PL APO 40X NA 1.30 CS2). An electro-optical modulator was used to adjust the

laser power at the entrance of the confocal system. The spectral acquisition was performed using an internal hybrid detector. Collected photons were dispersed by a prism and a specific motorized split mirror selecting the spectral detected band before the hybrid detector. Acquisitions were performed between 385 nm and 780 nm every 3 nm and with a spectral bandwidth of 5 nm.

Few milligrams of sample were deposited on a microscope slide. A cover slide was placed on the top of the sample and gently pressed on it.

Emission spectral profile: in order to check if the sample produces fluorescence, an emission spectral scan was performed. Typically, the sample is excited at a given wavelength (*e.g.* 1200 nm or 900 nm) while scanned through the emission wavelength (*e.g*. in the 385nm-780nm range). The SHG and THG should appear at the half and at the third of the excitation wavelength, respectively.

Results and Discussion

Structure solution and description

The structure solution was carried out using XRD data obtained from a red single crystal with a platelet shape. The unit cell parameters a=9.8307(6) Å, b=18.3900(11) Å, c=10.0023(5) Å and the space group *Cmce* (64) (where *e* denotes both *a* and *b* glide planes, *Cmca* notation is also used in the literature) were determined. The data collection and refinement details are given in table 1. The refinement was carried out with the JANA2006[20] software based on a structure solution obtained using the charge flipping method[21]. The EDS analysis of the single crystals led to the average atomic ratio 50.3/17.5/32.2 for S/V/Ba, respectively, in good agreement with the composition found at end of the refinement, *i.e.* $Ba_5V_2O_4S_8$. As will be discussed later, the formulation can be written $Ba_5(S_2)_2(VO_2S_2)_2$ to consider the structural units involved, see figure 1.

The original structure of $Ba_5(S_2)_2(VO_2S_2)_2$ is a rather opened framework that can be described by two alternating layers. The first layer is formed by disconnected VO_2S_2 tetrahedra separated from each other by the large Ba^{2+} cations. In the mixed anion tetrahedra, we find V1-S1= 2.178 (2) Å (two set of distances), V1-O1=1.663 (5) Å and V1-O2= 1.680 (5) Å. This particular heteroleptic environment is found in $K_3(VO_2S_2)$[22] and $Na_3(VO_2S_2)$[23] in which similar

V-O and V-S distances are found. In those phases the disconnected tetrahedra are separated by the alkaline cations. The second layer consists in disulfide pairs $(S_2)^{2-}$ surrounded by Ba atoms. The later delimit cavities in which the disulfide pairs are arranged in a 1D manner as depicted in figure 1. Along the *b* axis, the disulfide pairs are aligned following two parallel columns (1 and 2) shifted along *c* and *a* axis. The separation between the $(S_2)^{2-}$ pairs is of ~2.98 Å while a longer distance of 3.539 Å is found for S^{2-}–S^{2-} at $[VO_2S_2]$ vertices. The disulfide pairs exhibit distances $d_{S2\text{-}S2}$= 2.117(2) Å which are typical distances for $(S_2)^{2-}$ pairs. The three independent barium atoms are 8-coordinated with mixed ($Ba1O_2S_6$ and $Ba2O_4S_4$) or mono-anionic ($Ba3S_8$) environments. The sulfur atoms from (S_2) pairs are coordinated by four Ba atoms with distances in the range 3.103(1) – 3.341(1) Å slightly shorter in average than the Ba-S^{2-} as expected from the lower charge per sulfur atom in a $(S_2)^{2-}$ pair. It can be also illustrated by the difference between the persulfide BaS_2 (Ba surrounded by disulfide pairs) with the lowest d(Ba-S)~3.15 Å (up to 3.22 Å) and the sulfide BaS with d(Ba-S) ~ 3.194 Å.

Table 1. Data collection and refinement details

Formula	$Ba_5(S_2)_2(VO_2S_2)_2$
Molecular weight (g. mol^{-1})	1109.1
Symmetry	*orthorhombic*
Space group	*Cmce* (64)
Unit cell dimensions (Å)	a = 9.8307(6) b = 18.3900(11) c = 10.0023(5)
Volume ($Å^3$)	1808.28(18)
Z	4
Data Collection	
Equipment	Bruker D8 XRK900
λ [Ag K_α; Å]	0.56087
Calculated density (g cm^{-3})	4.0738
Crystal shape	Platelet
Crystal dimensions (μm)	0.06×0.04×0.01
Color	Red
Absorption correction	analytical
Scan mode	ω, φ
θ (min−max) (°)	2.21-35.51
μ (mm−1 ; for λ Kα = 0.56087Å)	6.636
F(000)	1944
Reciprocal space recording	−16 ≤ h ≤ 16

	−30 ≤ k ≤ 29
	−16 ≤ l ≤ 16
No. of measured reflections	38730
No. of independent reflections	2164
I > 3σ(I) (total)	1540
Refinement	
Number of refined parameters	52
Refinement method	Least-squares
Weighting scheme	sigma
R1(F) [I > 3σ(I)]/R1(F^2) (all data, %)	0.0288/0.0495
wR2(F^2) [I > 3σ(I)]/wR2(F^2) (all data, %)	0.0287/0.0392
Goodness of Fit	1.25
Max/Min residual electronic density (e^-/Å^3)	1.29/−1.28
Tmin / Tmax	0.6333 / 0.7456

Table 2. Atomic positions and isotropic thermal displacement for $Ba_5(S_2)_2(VO_2S_2)_2$

Atom	Wyck.	x	y	z	$U_{eq.}$
Ba1	8f	1/2	0.10825(2)	0.09128(4)	0.01388(11)
Ba2	8e	1/4	0.30635(2)	1/4	0.01119(10)
Ba3	4a	0	0	0	0.0230(2)
V1	8f	1/2	0.28574(6)	-0.02699(10)	0.0085(3)
S1	16g	0.68001(14)	0.34968(7)	-0.07497(13)	0.0171(3)
S2	16g	0.10767(14)	0.46087(7)	0.19892(13)	0.0160(3)
O1	8f	1/2	0.2069(2)	-0.1084(4)	0.0122(13)
O2	8f	1/2	0.2613(3)	0.1348(4)	0.0144(14)

Table 3. Anisotropic thermal parameters U_{ij} (Å²) for $Ba_5(S_2)_2(VO_2S_2)_2$

Atom	U_{11}	U_{22}	U_{33}	U_{12}	U_{13}	U_{23}
Ba1	0.0126(2)	0.0112(2)	0.0178(2)	0.00000	0.00000	0.0034(1)
Ba2	0.0100(2)	0.0124(2)	0.0112(2)	0.00000	-0.0001(1)	0.00000
Ba3	0.0414(5)	0.0125(3)	0.0150(3)	0.00000	0.00000	-0.0005(2)
V1	0.0085(5)	0.0085(5)	0.0086(4)	0.00000	0.00000	-0.0008(3)
S1	0.0118(6)	0.0158(6)	0.0237(6)	-0.0034(5)	0.0025(5)	-0.0006(5)
S2	0.0143(6)	0.0137(6)	0.0201(6)	0.0020(5)	-0.0013(5)	0.0011(4)
O1	0.014(3)	0.010(2)	0.012(2)	0.00000	0.00000	0.001(2)

O2	0.015(3)	0.017(2)	0.010(2)	0.00000	0.00000	-0.003(2)

Table 4. Main distances (Å) for $Ba_5(S_2)_2(VO_2S_2)_2$

Atoms 1,2	**d 1,2 (Å)**	**Atoms 1,2**	**d 1,2 (Å)**
Ba1—S1	3.244(1)×2	Ba3—S2	3.272(1)×4
Ba1—S2	3.103(1)×2	Ba3—S1	3.367(1)×4
Ba1—S2	3.341(1)×2		
Ba1—O1	2.698(5)	V1—S1	2.178(2)×2
Ba1—O2	2.848(5)	V1—O1	1.663(5)
Ba2—S2	3.208(1)×2	V1—O2	1.680(5)
Ba2—S1	3.431(1) ×2		
Ba2—S1	3.417(1) ×2	S2—S2	2.117(2)
Ba2—O1	2.847(2)×2		
Ba2—O2	2.838(2)×2		

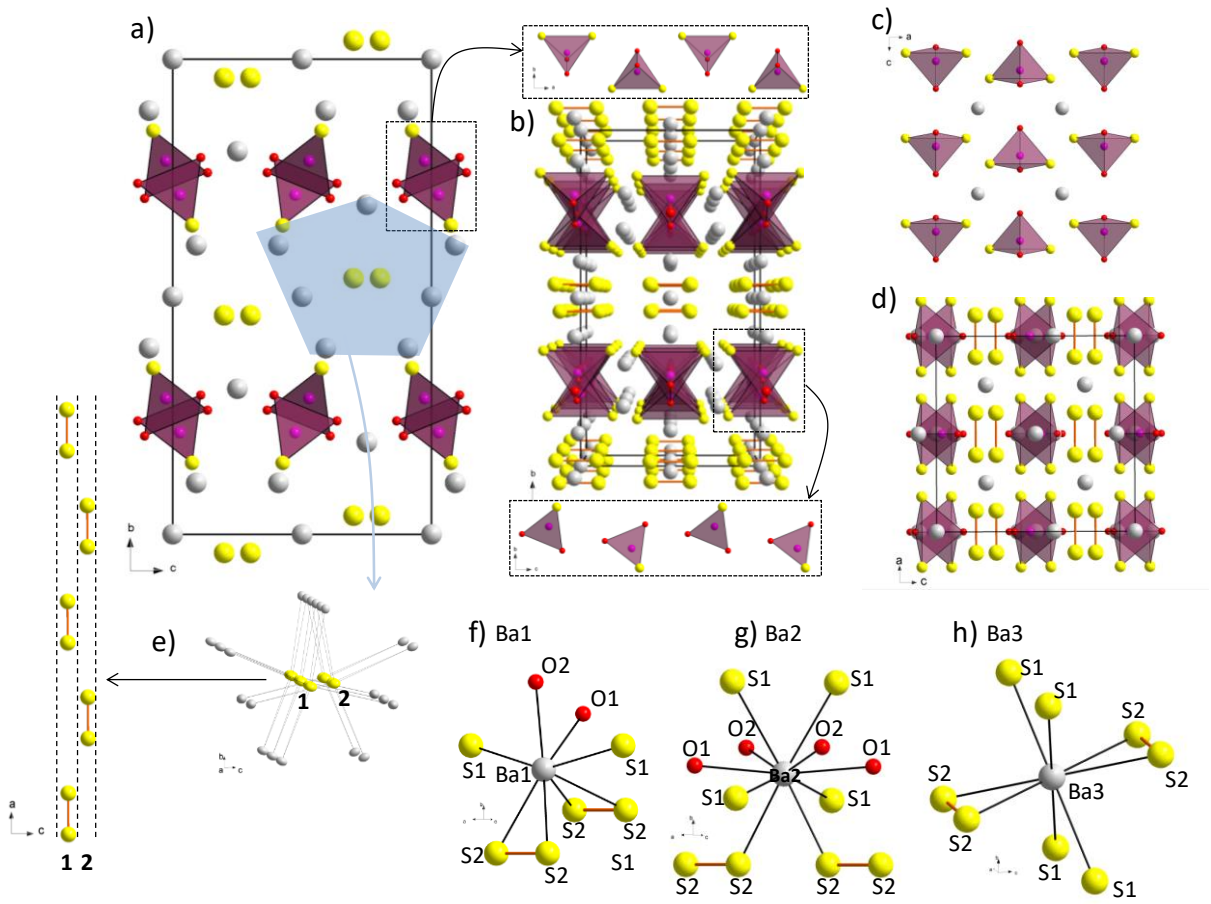

Figure 1. *a) Structure of $Ba_5(S_2)_2(VO_2S_2)_2$ projected along a axis, b) projection along c axis, c) slice of the structure showing the tetrahedra VO_2S_2 arrangement into a layer, d) other view of the structure highlighting the disulfide pairs channel along a, e) view of the disulfide pairs and the surrounding Ba atoms forming a channel around them and projection showing the 1D arrangement between the disulfide pairs, f-g-h) Ba atoms environments with Ba-S distances indicated and S-S bonds represented when present in their vicinity: Ba1, Ba2 and Ba3.*

Polycrystalline phase analysis

The synthesis of the pure powder phase was attempted following the procedure described in the experimental section. As depicted in figure 2a, the title phase is formed while the minor impurity $Ba_6(VO_2S_2)_2(VS_3O)(VS_4)$, for which the structure is discussed later as part of the Ba-V-S-O system, is identified. A multiphase Rietveld refinement using Jana2006[20] based on the single crystal structural model was carried out and led to very good reliability factors (R_{obs}= 0.0474, wR_{obs}= 0.0478, R_{all}= 0.0488, wR_{all}= 0.0481 and GOF= 1.48). The Rietveld quantification indicates the ratio 0.918(3)/0.082(3) for the title phase/impurity.

Relationship with other structure types in the Ba-V-S-O system

As mentioned above, the title phase represents the fifth member, to the best of our knowledge, in the quaternary system Ba-V-S-O which reveals complex and diversified structure types. The $Ba_{15}V_{12}S_{34}O_3$ phase[24] is formed of quasi-one-dimensional zigzag chains along the *c* axis connected by an oxygen atom. The chains are formed of face-sharing VS_6 octahedra and with VS_5O at the bends. The zigzag chains and their interconnection give rise to a lattice (layer) resembling a fence. The fence layers are stacked along the *a* axis. The cavities of the fence exhibit the mixed anion VS_3O tetrahedra. On another hand, $Ba_3V_2O_3S_4$ is a quasi-1D S=1 magnet and strongly correlated Mott insulator[25], with a cooperative polar arrangement of VO_3S units leading to the non-centrosymmetric space group $P6_3$. These units together with Ba^{2+}, separate $(VS_3)_\infty$ chains built from face-sharing $V^{3+}S_6$ octahedra. Considering the two above mentioned structure, they are quite different from the title phase which is exclusively made of unconnected $V^{5+}O_2S_2$ tetrahedra. Another major difference is the mixed valence state of the vanadium associated to magnetism in those reported phases. Common features can be found however in the remarkable phase $Ba_6V_4O_5S_{11}$ which exhibits different unconnected mixed anion tetrahedra that coexist separated by the Ba^{2+} cations, *i.e.* $Ba_6(VO_2S_2)_2(VS_3O)(VS_4)$, with VOS_3, VO_2S_2 (as found in our phase) and VS_4 units[26]. Finally, we have recently reported the orange oxysulfide $Ba_{10}V_6S_7O_{18}$, which can be written $Ba_{10}S(VO_3S)_6$ and crystallizes in the non-centrosymmetric $P6_3$ space group. It is formed of disconnected VO_3S tetrahedra separated by Ba^{2+} cations[27]. This phase represents a different structure type with a distinct symmetry but exhibits some similarities with the title phase, i.e. a framework with “channels” and unconnected oxysulfide tetrahedra. Then, the channels are occupied by isolated and disordered S^{2-} anions while we observe aligned disulfide pairs. On another hand, VO_3S tetrahedra are found versus VO_2S_2 in the title compound.

Optical measurements

The UV−visible diffuse reflectance analysis of the polycrystalline $Ba_5V_2O_4S_8$ is represented in Figure 2b. A Kubelka–Munk transformation[28] was applied to the measured diffuse reflectance (R) spectra using the function $F(R) = (1 - R)^2/2R$. Then a Tauc plot[29] was used to determine the

optical band gap E_g, using the equation, $(F(R)\cdot h\nu)^{1/n} = k(h\nu - E_g)$, where $h\nu$ is the photon energy, k an energy-independent constant, E_g the optical band gap and n, an exponent related to the type of transition. Assuming a direct allowed transition (exponent $n = ½$), the plot of $(F(R)\cdot h\nu)^2$ versus $h\nu$ allowed, after drawing a tangent line at the inflection point, to determine $E_g = 2.2$ eV. This is consistent with the observed red color of the crystals and the red-brownish powder.

DFT calculations

The total and projected densities of states are shown in figure 2d and focus in the region around the Fermi level of the valence band (VB) and the conduction band (CB). Within the VO_2S_2 building units, the vanadium atoms 3*d* states are lying in the conduction band starting from ~1.3 eV up to ~5.8 eV with the main contribution up to 3.7 eV approximatively. In the VB, the vanadium 3*d* states contribution is found roughly in the range -5 to -1 eV. They are hybridized with the O 2*p* and S 3*p* states of the VO_2S_2 building units. As expected from their electronegativity difference, O 2*p* has the strongest contribution lower in the VB (with the main large peak centered around -4.5 eV) and the $S_{(VO2S2)}$ 3*p* states is found mainly around -2.5 eV, *i.e.* higher in the VB. In a previous report[27], we have studied the projected density of states (PDOS) on the different mixed anion tetrahedra $V(O,S)_4$ found in $Ba_6(VO_2S_2)_2(VS_3O)(VS_4)$. It illustrates the evolution of their contributions higher in the VB when increasing the sulfur content (from $VO_3S \rightarrow VS_4$).

Concerning the sulfur atoms involved in the disulfide pairs, their contributions is distinct within the VB. Those isolated species exhibit more localized states in comparison with the other anions of the structure, S^{2-} and O^{2-} around vanadium. Just below the Fermi level, $(S_2)^{2-}$ 3*p* states dominate while S^{2-} involved in VO_2S_2 tetrahedra exhibit broader states lower in the VB as described above. Regarding the electronic structure description, the title phase may be decomposed as the combination of the structural entities $(Ba_5)^{10+}(S_2)_2{}^{4-}(VO_2S_2)_2)^{6-}$.

The electron localization function (ELF) has also been computed and allows the visualization of the nodal structure of the molecular orbital. The ELF maxima reflect localized electron pairs, in particular it allows investigating covalent bonds and Lone Pair electrons[30]. On figure 2c, a slice of the ELF clearly shows the covalent bonding between two sulfur atoms involved in a disulfide pairs.

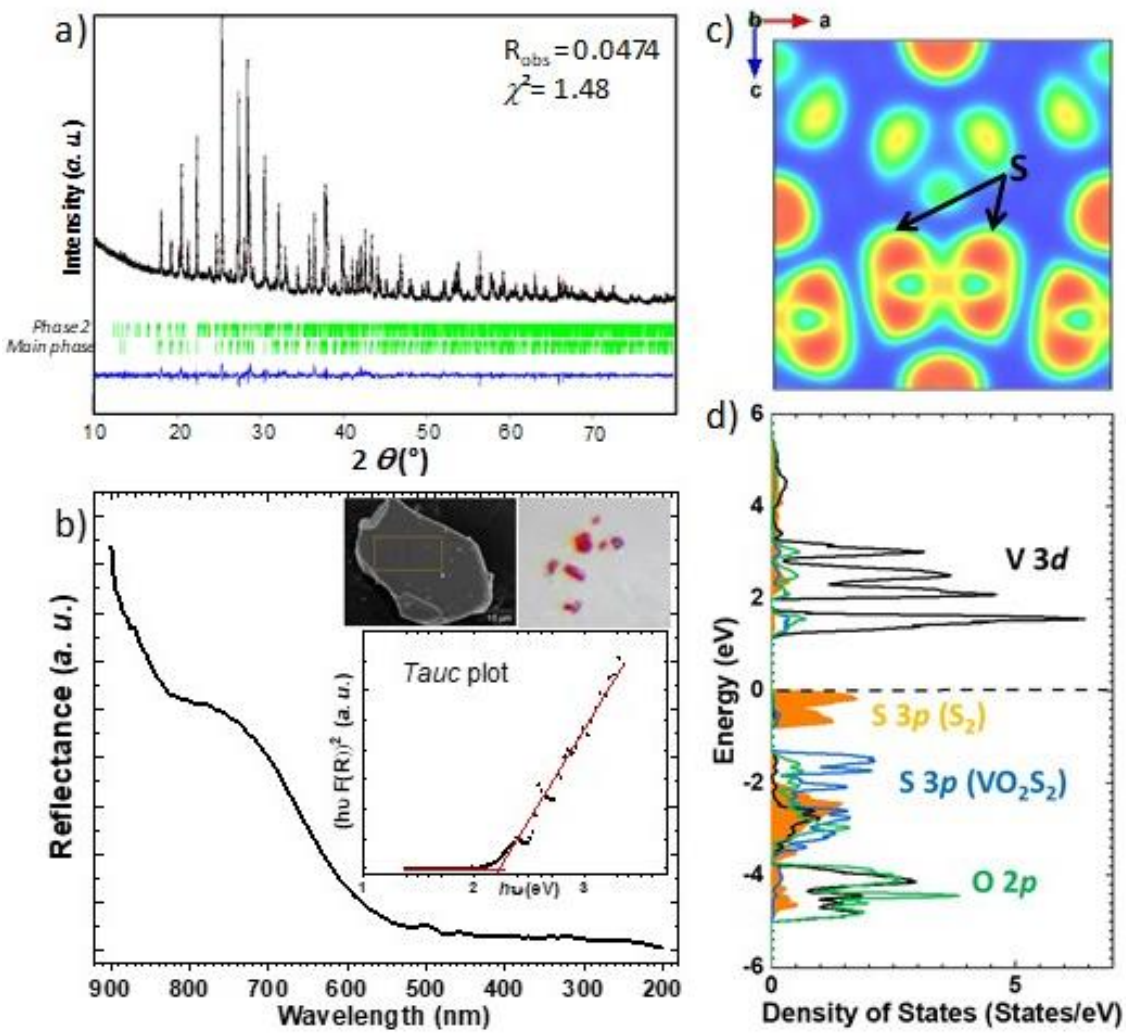

Figure 2. a) Powder XRD Rietveld refinement: the experimental pattern (black) and calculated pattern (red) are superimposed; the difference curve and the Bragg positions are represented in blue and green, respectively. b) Diffuse reflectance spectra with a *Tauc* plot as an inset to determine the experimental band gap; a picture of the reddish crystals and of a crystal SEM image are also shown as insets. c) DFT computed Electron Localization Function (ELF) with an S-S bond highlighted and d) the density of states (DOS) calculated for the title phase. The projected DOS is shown for the V (3d), O (2*p*) and S (3*p*) states. For the later, sulfur from the VO_2S_2 tetrahedra and sulfur from the disulfide pairs are distinguished. The Fermi level is set to 0.

Band gap engineering

Band gap engineering possibilities from an heteroleptic coordination at the transition metal site is particularly well illustrated in the $A_3(VO_{4-x}S_x)$ (A= Na^+, K^+, x= 0 to 4) phases, constituted of alkaline cations A^+ and disconnected $V(O_{4-x}S_x)$ tetrahedra. The variable O/S ratios lead to

colors ranging from white to deep red for $VO_4 \rightarrow VO_3S \rightarrow VO_2S_2 \rightarrow VOS_3 \rightarrow VS_4$. The cationic sub-lattice (Na^+ vs. K^+) and the symmetry differences impact the band gap. Besides, the S/O ratio of the $VO_{4-x}S_x$ tetrahedra seems to play a major role as shown from the DFT-GGA calculated band gaps of these series $A_3(VO_{4-x}S_x)$[23, 22]. From that assumption, we rationalized in a previous report the electronic structure of $Ba_{10}S(VO_3S)_6$ [27] in relation with its crystallo-chemical characteristics. In particular, we put forward the role of isolated S^{2-} that decrease the band gap compared to $A_3(VO_3S)$. Concerning the title phase, our DFT-GGA calculations with a similar level of approximation give a band gap of ~ 1.3 eV, underestimated as expected from the used functional. It compares better with the $A_3(VO_{4-x}S_x)$ (A= Na, K) phases exhibiting a higher ratio S/O (x>3) in $VO_{4-x}S_x$ tetrahedra than with the orange $A_3(VO_2S_2)$ phases due to the contribution of the disulfide pairs that lead to a narrower band gap.

They are a limited number of systems exhibiting such isolated sulfur species. They are found in the form of S^{2-} anions or of disulfide pairs $(S_2)^{2-}$ in $Ba_{12}In_4S_{19}$ [31] and BaFS [32] for instance, with a pivotal role in the band gap nature.

Considering other low dimensional systems, disulfide pairs are found in the layered phases $[A_2O_2](S_2)$ (A= La, Pr, Nd) [33] which are constituted by the alternative stack of fl!uorite-type $[A_2O_2]^{2+}$ layers and disulfide $(S_2)^{2-}$ layers arranged in a planar sheet. In particular, the $La_2O_2S_2$ phase (Fig. 3) crystallizes in the *Cmce* space group[34] with a band gap ~2.55 eV and exhibits photoluminescent properties upon doping[35].

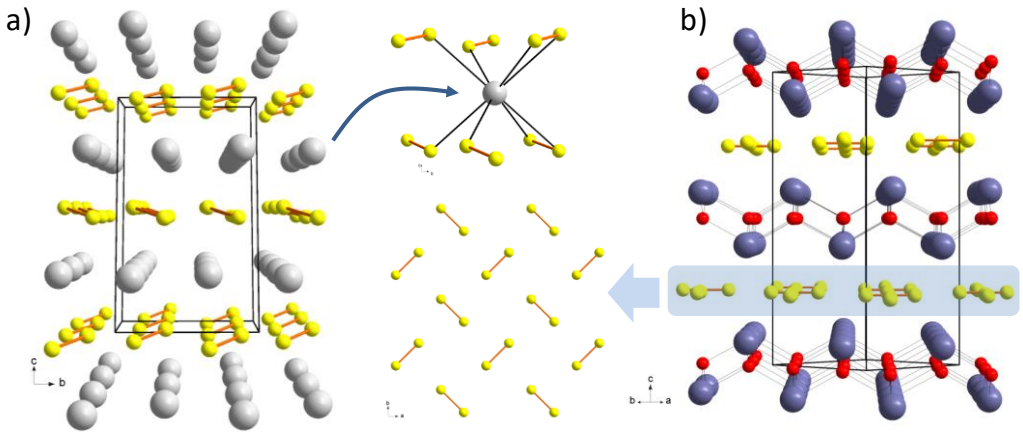

Figure 3. a) Structure of BaS_2 with emphasize on Ba environment exhibiting $d_{Ba\text{-}S}$ ranging from ~3.15 to 3.22Å and b) structure of the phase $La_2O_2S_2$ with a projection of disulfide layers showing the disulfide pairs 2D arrangement, each (S_2) is 90° rotated with respect to its neighbors.

Thermal stability

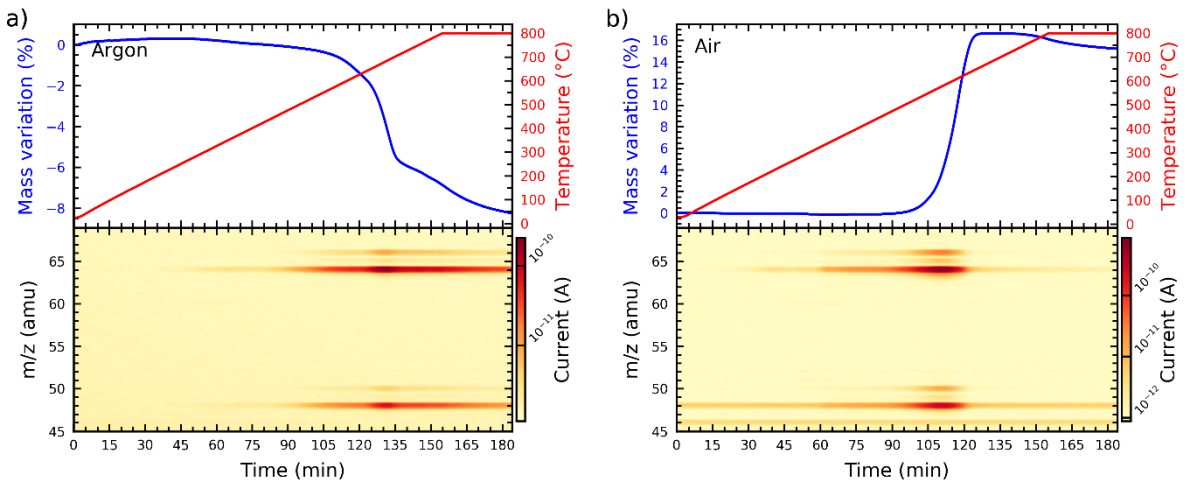

Figure 4: Thermogravimetric analysis (upper panes) coupled with mass spectrometry (lower panes) of $Ba_5(VO_2S_2)_2(S)_2$ a) under argon and b) under synthetic air. The mass variation and the temperature are given as a function of time.

The thermal stability of $Ba_5(VO_2S_2)_2(S)_2$ was investigated, under argon and air atmospheres, using thermogravimetric analysis coupled with mass spectrometry in the range 30 – 800 °C (Fig. 4). In both cases a very slow release of $SO_{2(g)}$ is observed for temperature higher than ~300 °C. The nature of the evolved gas is clearly identified by the signals measured at m/z = 64 amu (SO_2^+) and m/z = 48 amu (SO^+), interestingly we can rule out the evolution of hydrogen sulfide (m/z = 34 amu, not shown here). Under argon (Fig. 4-a), this decomposition process suddenly accelerates around 600 °C resulting in a sharp mass loss of 5.6 %, close to the theoretical mass loss expected for the loss of two sulfur atoms per formulae unit (5.78 %). Typically, it may correspond to a disulfide pair as would be expected from their specific reactivity (compared to S^{2-} within VO_2S_2 tetrahedra) as will be discussed later in the case of redox reactions. Then the observed mass loss would correspond to a $Ba_5V_2O_4S_6$ intermediary composition. In this case, if one disulfide pair is lost, the remaining one should break in a reductive process to form a compound with isolated S^{2-} anions in order to keep the charge balance if we consider preserved $V^{5+}O_2S_2$, i.e. $Ba_5(VO_2S_2)_2(S)_2$. If the remaining (S_2) is preserved, another scenario would be a reduction of vanadium, but in that case it should be accompanied by drastic structural changes as observed for instance after the ammonolysis of

$LaVO_4$ ($V^{5+}O_4$ disconnected tetrahedra) into the reduced Perovskite-type $LaVO_{2.78}N_{0.1}$ [36]. Further studies will be conducted to characterize this possible intermediate phase. Past 700 °C the decomposition of sulfur species continues at a slower rate. The XRD analysis of the residue show a decomposition into BaS, $Ba_3(VO_4)_3$ with a small amount of $Ba_6(VO_2S_2)_2(VS_3O)(VS_4)$ while some peaks remain unassigned and will be further investigated.

Under air (Fig. 4-b), the sudden evolution of $SO_{2(g)}$ is observed at a lower temperature of about 550 °C, the mass loss associated with the release of sulfur is however covered by the oxidation of sulfides to sulfates. The mass increases up to 16.7 % and stay stable from 650 – 750 °C, further heating results in the slow decomposition of the product. The stability of the mass in the 650 – 750 °C also point at a stable composition which still need to be elucidated. The XRD analysis of the residue shows a full decomposition into $BaSO_4$ and V_2O_5.

It is interesting to mention the new and reversible topochemical route for copper insertion into $(Q_2)^{2-}$ (*Q*=S, Se) dimers to design layered transition metal chalcogenides using low-temperatures[37]. In particular copper was inserted in the $(S_2)^{2-}$-containing phases $La_2O_2S_2$ and $Ba_2F_2S_2$ to form the corresponding layered copper chalcogenides. Remarkably, the redox centers upon Cu insertion are the chalcogen pairs. Our phase should be an interesting precursor for such topotactic modifications.

Considering other possible reactions, one can also imagine a reaction that may lead to an original phase exclusively formed of VO_2S_2 building blocks and Ba^{2+} atoms that should have an increased band gap, i.e. $Ba_5(VO_2S_2)_2(S)_2 \rightarrow 2BaS_2 + Ba_3(VO_2S_2)_2$.

Electron microscopy

We have also performed electron diffraction experiments to probe the structure at a different scale, see figure 5. According to the work of Morniroli[38], the comparison of the difference of periodicity and shift between the zero (ZOLZ) and first order Laue zone (FOLZ) of the [010], [100], [001] zone axis electron diffraction pattern for the orthorhombic system leads to an extinction symbol. The determined extinction symbol gives the Bravais lattice and other information such as the existence of a glide plane. This information helps for the determination of the space group. In our case, the extinction symbol is *C* - - *e* (- means no glide plan). The analysis of this particular crystallite indicates no glide plane. A rotation along the basic axis (a, b, c) indicates a screw 2_1 axis along c. This is consistent with the non-

centrosymmetric (NCS) space group Cm2e and with the space group Cmme. Moreover, from the XRD single crystal analysis, those space groups are not relevant since no reflection violating the *c* glide plane (l= 2n+1) can be detected in the (h0l) plan presented on figure 5d from our XRD data). Then, the reconstitution of the reciprocal space in diffraction, which allows confirming the cell parameters as well as highlighting the extinction conditions and supplementary structural phenomenon like superstructure, was not possible because the sample is very sensitive to the beam. It prevents any high resolution imaging to further analyze the structure and eventually reveal very local structural information like order, disorder *etc*…. From this study, one can deduce a possible reactivity of the sample or the potential occurrence of non-centrosymmetric crystallites or domains. This will be further investigated in next section.

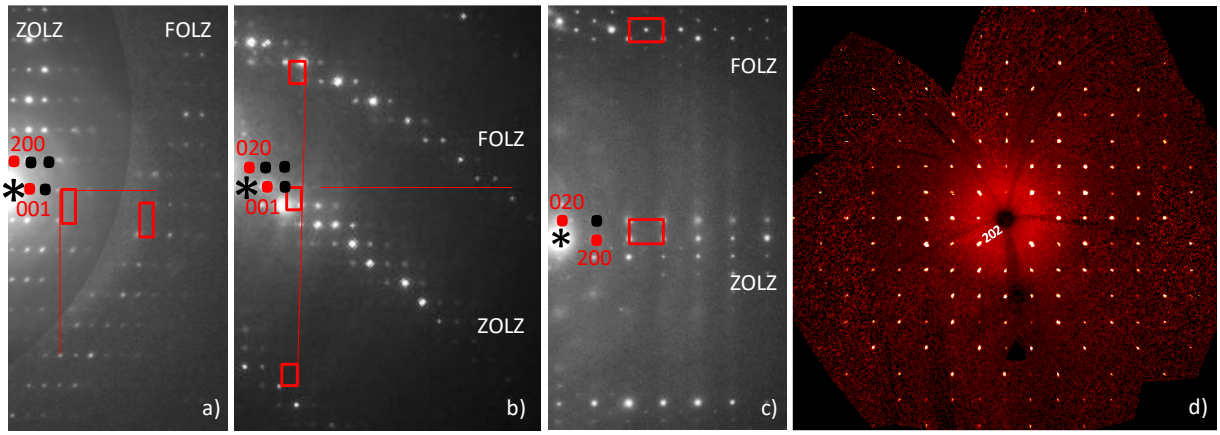

Figure 5. Electron diffraction patterns: comparison between the zero and first order Laue Zone (ZOLZ and FOLZ) in the a) [010] b) [100] and c) [001] zone axis pattern. The deducted extinction is C - - a or C- - b. d) (h0l) plan from single crystal XRD data collection.

Non-linear optical properties

SHG measurements were carried out, initially to investigate possible non-centrosymmetric contribution in the polycrystalline sample regarding electron microscopy results. Bright field and SHG images for excitation of $Ba_5(VO_2S_2)_2(S)_2$ at 900 nm are presented in **Erreur ! Source du renvoi introuvable.**. The emission spectrum (integrated over the whole field of view) is plotted in Figure .

First, we note that the emission spectrum exhibits a typical SHG peak (half of the excitation wavelength, *i.e.* 450 nm) and a fluorescence emission mainly in the 500 nm -750 nm range.

SHG and fluorescence, are however relatively low and seems to decrease with exposure time. More into details, the THG intensity only decreases by 10% in circa 3 sec and then remains constant under laser irradiation while SHG intensity is divided by 2.5 in circa 10 sec. This could be due to a chemical pollution partially degraded under laser beam. For an excitation wavelength of 1200 nm, behavior for SHG evolution is similar to the excitation at 900 nm.

Second, on figure 6b and 6c, it clearly appears that the SHG emission is not homogeneously distributed over the sample (sparsely distributed spots). To go deeper into this observation, the emission spectra from different regions of interest (ROI) marked by squares in **Erreur ! Source du renvoi introuvable.** were plotted in Figure 8. One can notice two main different spectra: (i) Spectra with strong SHG emission for ROI2 and ROI3 and (ii) Spectra with no SHG emission and only fluorescence in the 500 nm -750 nm range for ROI1 and ROI4. It means that the particles constituting the sample mainly correspond to a centrosymmetric crystalline phase whereas the SHG signal detected is mainly due to particular zones of non-centrosymmetry. The SHG signal could then be attributed to impurities (a possible explanation could be the presence of quartz slivers, observed with a binocular and stemming from the synthetic procedure). Nevertheless, regarding electron microscopy results, we cannot exclude that the SHG spots might arise from a non-centrosymmetric phase close but different from the predominant centrosymmetric $Ba_5(VO_2S_2)_2(S)_2$ crystalline phase either structurally (polymorph) or chemically (derivative).

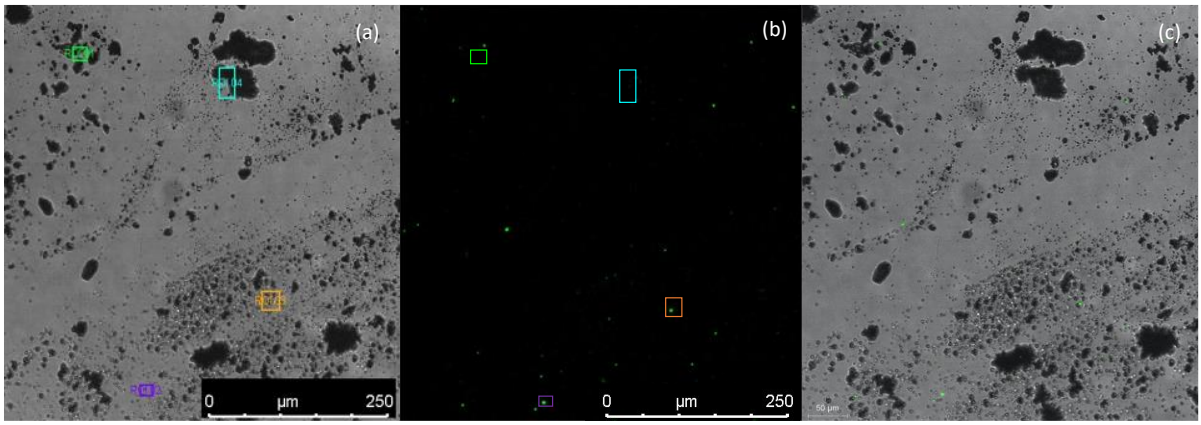

Figure 6. $Ba_5(VO_2S_2)_2(S)_2$ Bright Field (a), SHG (b) and overlay of both (c) images for excitation at 900 nm. ROI are represented by squares.

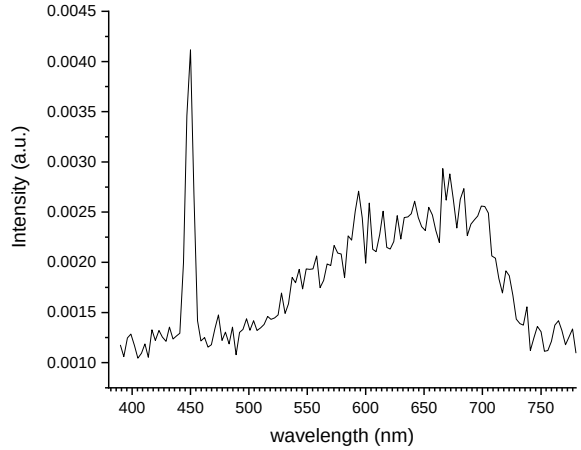

Figure 7. Emission spectrum of $Ba_5(VO_2S_2)_2(S)_2$ for excitation at 900 nm.

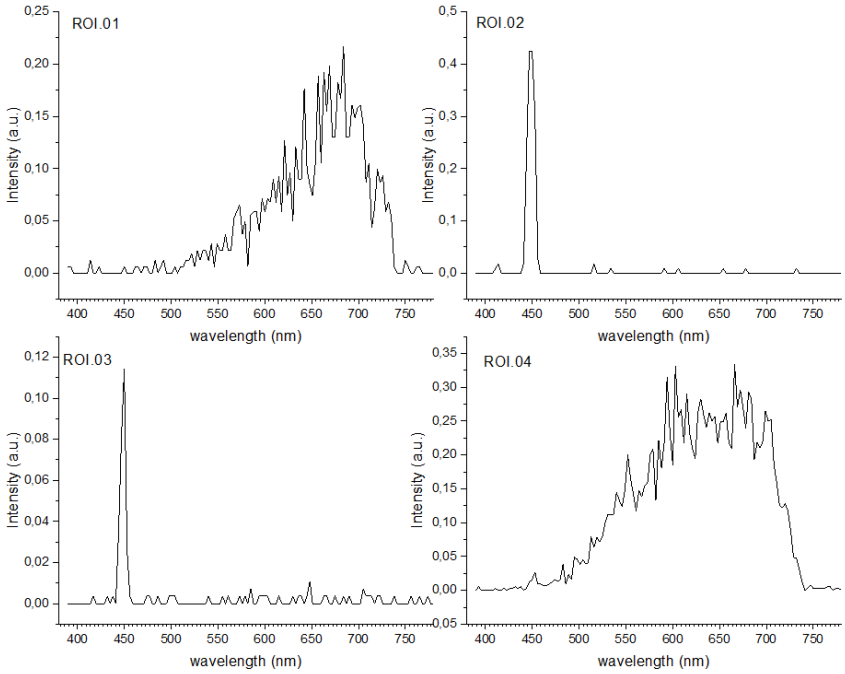

Figure 8. Emission spectra from ROIs in $Ba_5(VO_2S_2)_2(S)_2$ for excitation at 900 nm.

Third Harmonic Generation (THG) signal was also recorded and is evenly distributed across the sample as shown in Figure . One should recall that THG is not restricted to NCS structures and can occur either in centrosymmetric or NCS structures. Figure clearly shows a THG peak at 400 nm on the emission spectrum of the sample for excitation at 1200 nm.

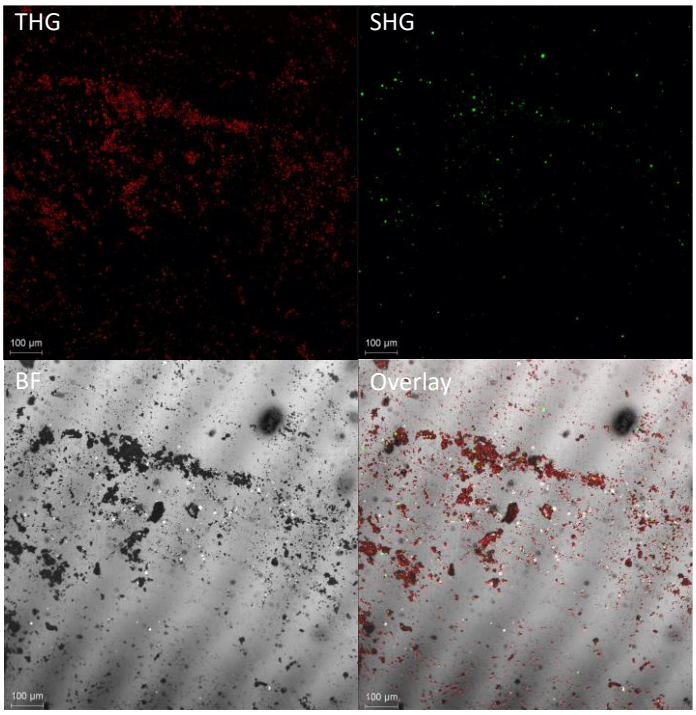

Figure 9. THG, SHG, BF and overlay of both (right image) of $Ba_5(VO_2S_2)_2(S)_2$ for excitation at 1200 nm

More into details, over the whole field of view, the ratio THG/SHG is 14. The conversion efficiency of THG is usually much lower than SHG[39]. The fact that THG is much higher than SHG also supports the assumption of a pollution of the sample. These observations are thus consistent with the centrosymmetric *Cmce* space group determined from XRD for $Ba_5(VO_2S_2)_2(S)_2$ which excludes the application of this phase for frequency doubling.

However, an interesting feature of this compound is its relatively high third-harmonic generation (THG) signal. Such non-linear optical properties have been for instance reported in centrosymmetric Cu_2O crystals which have shown large third-order susceptibility and third-harmonic generation[40]. To cite a few other inorganic crystalline solids**,** THG has also been investigated in other oxides such as $LiKB_4O_7$ [41] or the centrosymmetric rutile TiO_2 ($P4_2/mnm$) with efficient triple photon generation [15]. In non-oxides, the fluoride $BaMgF_4$ [42] has recently shown the highest direct UV-third harmonic generation conversion efficiency in a solid state system via pure $\chi^{(3)}$ nonlinear process. In the chalcogenide phases $Ag_xGa_xGe_{1-x}Se_2$, THG have been related to the anions coordination within (Ga, Ge)Se_4 tetrahedra and their resulting dipole moments that define the optical nonlinearities [43]. In our case, we report interesting THG properties in a crystalline oxychalcogenide, which to the best of our knowledge is rather uncommon for this type of crystalline materials.

More into details, we have performed a comparison of THG intensity emitted by Cu_2O, known for its high THG signal as mentioned above, and $Ba_5(VO_2S_2)_2(S)_2$ powdered samples. Emission spectra of Cu_2O and $Ba_5(VO_2S_2)_2(S)_2$ for excitation at 1200 nm are plotted in Figure. The peak at 400 nm is attributed to third harmonic generation of the samples. One can notice fluorescence of the samples in the 580 nm – 720 nm range. The average THG signal generated by the $Ba_5(VO_2S_2)_2(S_2)_2$ powder sample is approximately twice lower than the THG signal of a Cu_2O also in the powder form. In the light of this information, $Ba_5(VO_2S_2)_2(S_2)_2$ single-crystal is prone to exhibit interesting 3rd order nonlinear properties.

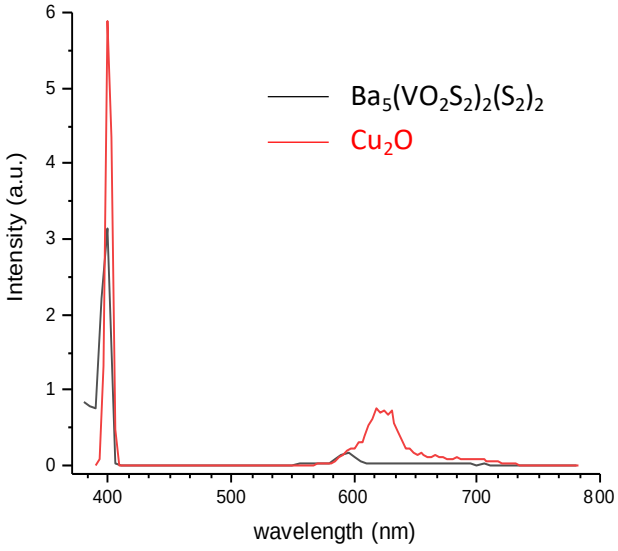

Figure 10. Emission spectra of Cu_2O and $Ba_5(VO_2S_2)_2(S)_2$ for excitation at 1200 nm

Conclusion

The new oxysulfide $Ba_5(VO_2S_2)_2(S)_2$ was identified and its structure solved in the space group *Cmce*. It represents an original member, the fifth, in the quaternary system Ba-V-S-O. This phase exhibits the mixed anion building units VO_2S_2 and isolated disulfide pairs. The DFT study show that the $(S_2)^{2-}$ 3*p* states found just below the Fermi level dictate the band gap while the other anions involved in VO_2S_2 tetrahedra and in particular S^{2-} anions exhibit broader states lower in the VB. The rationalization of the structure with respect to the electronic structure show all the interest of designing new phases using such mixed anion building blocks and/or disulfide pairs. In particular, band gap engineering trough mastered approaches is important for a variety of properties. Despite the absence of second harmonic generation stemming from

the existence of a center of inversion in the crystal structure, we show in this new phase third-harmonic generation properties. To the best of our knowledge, this is rather uncommon in oxychalcogenide or mixed anion crystalline solids. Thus, $Ba_5(VO_2S_2)_2(S)_2$ deserves further investigations in order to fully access the nonlinear optical $\chi^{(3)}$ coefficients. This will be crucial to evaluate its potential for nonlinear optical applications.

Supporting Information: The Supporting Information contain the unit cell parameters and atomic coordinates of the optimized structure

Crystal structure report

CCDC Deposition Number 1969802 contains the supplementary crystallographic data for this paper. The data can be obtained free of charge from The Cambridge Crystallographic Data Centre via https://www.ccdc.cam.ac.uk/structures

Acknowledgments

This study was supported by the French government through the Programme Investissement d'Avenir (I-SITE ULNE / ANR-16-IDEX-0004 ULNE) managed by the Agence Nationale de la Recherche (Project ANION-COMBO). X-Rays Diffractometers and Transmission Electronic Microscopy are funded by Région NPDC, FEDER, CNRS and MESR. The regional computational cluster supported by Lille University, CPER Nord-Pas-de-Calais/CRDER, France Grille CNRS and FEDER is thanked for providing computational resources. B. Almoussawi thanks University of Lille for financial support. Region Normandie and the European regional development fund (FEDER) are acknowledged for their financial support (SCAMPI Project) that enables SHG Microscopy experiments.

REFERENCES

[1] Kageyama, H.; Hayashi, K.; Maeda, K.; Attfield, J.-P.; Hiroi, Z.; Rondinelli, J. M.; Poeppelmeier, K. R. Expanding frontiers in materials chemistry and physics with multiple anions. *Nature Communications* **2018**, 9(1), 772.

[2] Ahmed, M.; Xinxin, G. A. Review of Metal Oxynitrides for Photocatalysis. *Inorg. Chem. Front.* **2016**, 3 (5), 578–590.

[3] Kim, S.-W.; Pereira, N.; Chernova, N. A.; Omenya, F.; Gao, P.; Whittingham, M. S.; Amatucci, G. G.; Su, D.; Wang, F. Structure Stabilization by Mixed Anions in Oxyfluoride Cathodes for High-Energy Lithium Batteries. *ACS Nano* **2015**, 9 (10), 10076–10084.

[4] Muhammady, S.; Kurniawan, Y.; Ishiwata, S.; Rousuli, A.; Nagasaki, T.; Nakamura, S.; Sato, H.; Higashiya, A.; Yamasaki, A.; Hara, Y.; et al. Electronic and Thermoelectric Properties of Layered Oxychalcogenides (BiO)CuCh (Ch = S, Se, Te). *Inorg. Chem.* **2018**, 57 (16), 10214–10223.

[5] Kabbour, H.; Janod, E.; Corraze, B.; Danot, M.; Lee, C.; Whangbo, M.-H. and Cario, L. Structure and Magnetic Properties of Oxychalcogenides $A_2F_2Fe_2OQ_2$ (A= Sr, Ba; Q= S, Se) with Fe_2O Square Planar Layers Representing an Antiferromagnetic Checkerboard Spin Lattice. *J. Am. Chem. Soc.* **2008**, 130, 8261–8270.

[6] Blandy, J. N.; Liu, S.; Smura, C. F.; Cassidy, S. J.; Woodruff, D. N.; McGrady, J. E.; Clarke, S. J. Synthesis, Structure, and Properties of the Layered Oxide Chalcogenides Sr2CuO2Cu2S2 and $Sr_2CuO_2Cu_2Se_2$. *Inorg. Chem.* **2018**, 57 (24), 15379–15388. b) Lü, M.; Mentré, O.; Gordon, E. E.; Whangbo, M.-H.; Wattiaux, A.; Duttine, M.; Tiercelin, N.; Kabbour, H. A Comprehensive Study of Magnetic Exchanges in the Layered Oxychalcogenides $Sr_3Fe_2O_5Cu_2Q_2$ (Q=S, Se). *Journal of Magnetism and Magnetic Materials* **2017**, 444, 147–153.

[7] Luu, S. D. N.; Vaqueiro, P. Layered Oxychalcogenides: Structural Chemistry and Thermoelectric Properties. *Journal of Materiomics* **2016**, 2 (2), 131–140.

[8] a) Miura, A.; Oshima, T.; Maeda, K.; Mizuguchi, Y.; Moriyoshi, C.; Kuroiwa, Y.; Meng, Y.; Wen, X.-D.; Nagao, M.; Higuchi, M.; et al. Synthesis, Structure and Photocatalytic Activity of Layered $LaOInS_2$. *J. Mater. Chem. A* **2017**, 5 (27), 14270–14277. b) Kabbour, H. ; Sayede, A. ; Saitzek, S. ; Lefèvre, G. ; Cario, L. ; Trentesaux, M. and Roussel, P. Structure of the water-splitting photocatalyst oxysulfide α-$LaOInS_2$ and ab initio prediction of new polymorphs. *Chemical Communications* **2020,** 56, 1645.

[9] Kuriki, R.; Ichibha, T.; Hongo, K.; Lu, D.; Maezono, R.; Kageyama, H.; Ishitani, O.; Oka, K.; Maeda, K. A Stable, Narrow-Gap Oxyfluoride Photocatalyst for Visible-Light Hydrogen Evolution and Carbon Dioxide Reduction. *J. Am. Chem. Soc.* **2018**, 140 (21), 6648–6655.

[10] Liu, B. W.; Jiang, X.-M; Wang, G.-E; Zeng, H.-Y.; Zhang, M.-J.; Li, S.-F.; Guo, W.-H.; Guo, G.-C. Oxychalcogenide BaGeOSe2: Highly Distorted Mixed-Anion Building Units Leading to a Large Second-Harmonic Generation Response. *Chem. Mater.* **2015**, 27, 24, 8189-8192.

[11] Tsujimoto, Y.; Juillerat, C. A.; Zhang, W.; Fujii, K.; Yashima, M.; Halasyamani, P. Shiv.; zur Loye, H.-C. Function of Tetrahedral ZnS_3O Building Blocks in the Formation of $SrZn_2S_2O$: A Phase Matchable Polar Oxysulfide with a Large Second Harmonic Generation Response. *Chem. Mater.* **2018**, 30 (18), 6486–6493.

[12] Hongil, J.; Kim, H.-G.; Byun, H.-R.; Jang, J. I., Ok, K. M. Synthesis, structure, and third-harmonic generation measurements of a mixed alkali metal iodate, $KLi_2(IO_3)_3$. *Journal of Solid State Chemistry*, **2020**, 282, 121120.

[13] Boyd, R, W. Nonlinear Optics; 3rd Edition, Academic Press: San Diego USA, **2008**

[14] Hübel, H.; Hamel, D. R.; Fedrizzi, A.; Ramelow, S.; Resch, K. J.; Jennewein, T. Direct generation of photon triplets using cascaded photon-pair sources. *Nature* **2010**, 466, 601

[15] Gravier, F. and Boulanger, B. Cubic parametric frequency generation in rutile single crystal. *Optics Express* **2006**, 14, 11715

[16] Blöchl, P. E. Projector Augmented-Wave Method. *Phys. Rev. B* **1994**, 50 (24), 17953–17979.

[17] Kresse, G.; Joubert, D. From Ultrasoft Pseudopotentials to the Projector Augmented-Wave Method. *Phys. Rev. B* **1999**, 59 (3), 1758–1775.

[18] G. Kresse et al.: Vienna ab-initio simulation package (VASP), https://www.vasp.at

[19] Perdew, J. P.; Burke, K.; Ernzerhof, M. Generalized Gradient Approximation Made Simple. *Phys. Rev. Lett.* **1996**, 77 (18), 3865–3868.

[20] Petříček, V.; Dušek, M.; Palatinus, L. Crystallographic Computing System JANA2006: General Features. Zeitschrift für Kristallographie - *Crystalline Materials* **2014**, 229 (5), 345–352.

[21] Lee, A. van der. Charge Flipping for Routine Structure Solution. *J. Appl. Cryst.* **2013**, 46 (5), 1306–1315.

[22] Schnabel, S.; Röhr, C. Kalium-Thio/Oxo-Vanadate(V) K3[VSxO4–x] (x = 1–4) Und Na3[VSO3]: Synthese, Strukturchemie, Eigenschaften. *Zeitschrift für Naturforschung B* **2014**, 63 (7), 819–833.

[23] Schnabel, S.; Röhr, C. Gemischte Thio/Oxo-Orthovanadate Na3[VSxO4 –x] (x = 2, 3): Darstellung – Strukturen – Eigenschaften / Mixed Thio/Oxo Orthovanadates Na3[VSxO4−x] (x = 2, 3): Synthesis – Crystal Structures – Properties. *Zeitschrift für Naturforschung B* **2014**, 60 (5), 479–490.

[24] Wong, C. J.; Hopkins, E. J.; Prots, Y.; Hu, Z.; Kuo, C.-Y.; Pi, T.-W.; Valldor, M. Anionic Ordering in $Ba_{15}V_{12}S_{34}O_3$, Affording Three Oxidation States of Vanadium and a Quasi-One-Dimensional Magnetic Lattice. *Chem. Mater.* **2016**, 28 (6), 1621–1624.

[25] Hopkins, E. J.; Prots, Y.; Burkhardt, U.; Watier, Y.; Hu, Z.; Kuo, C.-Y.; Chiang, J.-C.; Pi, T.-W.; Tanaka, A.; Tjeng, L. H.; Valldor, M. $Ba_3V_2S_4O_3$: A Mott Insulating Frustrated Quasi-One-Dimensional S=1 Magnet. *Chemistry A European Journal* **2015**, 28, 7938-7943.

[26] Litteer, J. B.; Fettinger, J. C.; Eichhorn, B. W. $Ba_6V_4O_5S_{11}$. *Acta Crystallographica Section C* **1997**, 53 (2), 163–165.

[27] Nicoud, S.; Mentré, O.; Kabbour, H. The $Ba_{10}S(VO_3S)_6$ Oxysulfide: One-Dimensional Structure and Mixed Anion Chemical Bonding. *Inorg. Chem.* **2019**, 58 (2),1349–1357.

[28] a) Tauc, J. *Optical Properties of Solids*, F. Abeles ed. 1972, North-Holland. b) Tauc, J.; Grigorovici, R. and Vancu, A. Optical Properties and Electronic Structure of Amorphous Germanium. *Phys. Status Solidi* 1966, 15, 627.

[29] a) Wendlandt, W.; Hecht, H. G. Reflectance Spectroscopy. New York; London Interscience, 1966. b) Kubelka, P.; Munk, F. Z. *Ein Beitrag Zur Optik Der Farbanstriche*. Tech. Phys. 1931, 11, 593–601.

[30] Silvi, B.; Savin, A. Classification of Chemical Bonds Based on Topological Analysis of Electron Localization Functions. *Nature* **1994**, 371 (6499), 683–686.

[31] Liu, J.-W.; Wang, P.; Chen, L. Contribution of Disulfide S22– Anions to the Crystal and Electronic Structures in Ternary Sulfides, $Ba_{12}In_4S_{19}$, $Ba_4M_2S_8$ (M = Ga, In). *Inorg. Chem.* **2011**, 50 (12), 5706–5713.

[32] Driss, D.; Cadars, S.; Deniard, P.; Mevellec, J.-Y.; Corraze, B.; Janod, E.; Cario, L. Crystal Structure and Chemical Bonding in the Mixed Anion Compound BaSF. *Dalton Trans.* **2017**, 46 (46), 16244–16250.

[33] Wichelhaus, W. The Rare-Earth Oxide Disulfides $La_2O_2S_2$, $Pr_2O_2S_2$, and $Nd_2O_2S_2$. *Naturwissenschaften* **1978**, 65, 593–594.

[34] Ostoréro, J.; Leblanc, M. Room-Temperature Structure of $La_2O_2S_2$. *Acta Cryst.* C **1990**, 46 (8), 1376–1378.

[35] Bera, D.; Maslov, S.; Qian, L.; Holloway, P. H. Low-Temperature Synthesis of Red-Emitting Nanostructured $La_2O_2S_2$:Eu^{3+} Phosphor. *Solid State Communications* **2011**, 151 (2), 164–168.

[36] Yoon, S.; Maegli, A. E.; Karvonen, L.; Shkabko, A.; Populoh, S.; Gałązka, K.; Sagarna, L.; Aguirre, M. H.; Jakes, P.; Eichel, R. A.; et al. Synthesis, Crystal Structure, Electric and Magnetic Properties of LaVO2.78N0.10. *Zeitschrift für anorganische und allgemeine Chemie* **2014**, 640 (5), 797–804.

[37] Sasaki, S.; Driss, D.; Grange, E.; Mevellec, J.-Y.; Caldes, M. T.; Guillot-Deudon, C.; Cadars, S.; Corraze, B.; Janod, E.; Jobic, S.; et al. A Topochemical Approach to Synthesize Layered Materials Based on the Redox Reactivity of Anionic Chalcogen Dimers. *Angewandte Chemie International Edition* **2018**, 57 (41), 13618–13623.

[38] Morniroli, J. P.; Steeds, J. W. Microdiffraction as a Tool for Crystal Structure Identification and Determination. *Ultramicroscopy* 1992, 45 (2), 219–239. https://doi.org/10.1016/0304-3991(92)90511-H.

[39] Sauter, E. G. Nonlinear Optics; John Wiley & Sons, **1996**.

[40] Mani, S. E.; Jang, J. I.; Ketterson, J. B. Large Third-Order Susceptibility and Third-Harmonic Generation in Centrosymmetric Cu_2O Crystal. *Opt. Lett.* **2009**, 34 (18), 2817–2819.

[41] B. Kulyk, V. Kapustianyk, Ya. Burak, V. Adamiv, B. Sahraoui. Third harmonic generation in $LiKB_4O_7$ single crystal. *Materials Chemistry and Physics* 120 (**2010**) 114–117

[42] Mateo, L.; Ramírez, M. O.; Carrasco, I.; Molina, P.; Galisteo-López, J. F.; Víllora, E. G.; De las Heras, C.; Shimamura, K.; Lopez, C. and Bausá, L. E. $BaMgF_4$: An Ultra-Transparent Two-Dimensional Nonlinear Photonic Crystal with Strong $\chi^{(3)}$ Response in the UV Spectral Region. *Adv. Funct. Mater.* **2014**, *24*, 1509–1518.

[43] Krymus, A.S.; Myronchuk, G.L.; Parasyuk, O.V.; Lakshminarayana, G.; Fedorchuk, A.O.; El-Naggar, A.; Albassam, A.; Kityk, I.V. Photoconductivity and nonlinear optical features of novel $Ag_xGa_xGe_{1-x}Se_2$ crystals. *Materials Research Bulletin* **2017**, 85, 74–79

TOC

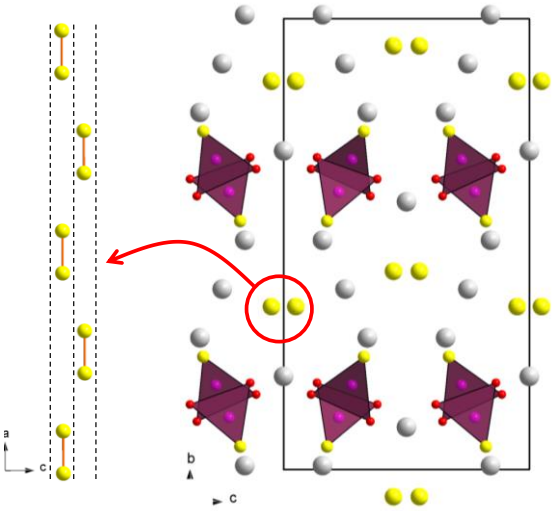

SYNOPSIS

$Ba_5(VO_2S_2)_2(S_2)_2$ is an original oxysulfide which exhibits mixed anion unconnected tetrahedra $V^{5+}O_2S_2$ and isolated disulfide pairs $(S_2)^{2-}$ arranged in a 1D. The electronic structure below the Fermi level is dominated by the disulfide 3*p* states which dictate the band gap. We point out *anionic* tools for band gap engineering, which can be useful to design phases for numerous applications. In this study, we show promising third harmonic generation properties.